# We are IntechOpen, the world's leading publisher of Open Access books Built by scientists, for scientists

**4,800**
Open access books available

**122,000**
International authors and editors

**135M**
Downloads

Our authors are among the

**154**
Countries delivered to

**TOP 1%**
most cited scientists

**12.2%**
Contributors from top 500 universities


WEB OF SCIENCE™

Selection of our books indexed in the Book Citation Index in Web of Science™ Core Collection (BKCI)

## Interested in publishing with us?
## Contact book.department@intechopen.com

Numbers displayed above are based on latest data collected.
For more information visit www.intechopen.com

# 10

# Wave Propagation from a Line Source Embedded in a Fault Zone

Yoshio Murai
*Hokkaido University*
*Japan*

## 1. Introduction

The major crustal faults are not a single fault but form fault zones. The fault zone consists of several fault segments (e.g., Tchalenko, 1970; Tchalenko & Berberian, 1975). Each fault segment contains many cracks on a small scale. It is revealed from analyses of shear-wave splitting and P-wave polarization anomalies that parallel cracks are densely distributed in a fault zone (Leary et al., 1987; Li et al., 1987). Televiewer observations in boreholes also reveal the presence of a distribution of parallel cracks within a fault zone (Malin et al., 1988; Leary et al., 1987). Moreover it is revealed from seismic observations that a fault zone is characterized as a lower velocity zone than the surrounding intact rocks (Mooney & Ginzburg, 1986) and low-Q area (Kurita, 1975; Li et al., 1994). When an earthquake occurs in the fault zone, the following seismic waveforms are observed in the fault zone: the P and S headwaves refracted along the cross-fault material contrast (Ben-Zion & Malin, 1991; Hough et al., 1994) and seismic waves trapped in a low-velocity zone (e.g., Li & Leary, 1990; Li et al., 1994). It is important to determine the fault zone structure for the purposes of earthquake prediction and strong motion prediction. It is necessary to achieve it that the observational data should be simulated by means of theoretical studies.

In this study, we compute synthetic seismograms of the displacement field radiated from a seismic source embedded in a fault zone in order to simulate fault zone trapped waves. We assume a low-velocity zone and/or a zonal distribution of parallel cracks as a fault zone and investigate SH wave propagation in a 2-D elastic medium. We use the method introduced by Murai & Yamashita (1998) for the zonal distribution of parallel cracks. This method of analysis has advantages that multiple elastic wave scattering due to a large number of densely distributed cracks is easily treated and that the velocity contrast can be easily introduced. Finally, we try to simulate the fault zone trapped waves observed by Li et al. (1994) and estimate the crack size and the density of crack distribution.

## 2. Models of a fault zone

We assume following five models as a fault zone as shown in Fig. 1.

1. A zone of densely distributed parallel cracks (Fig. 1a). All the cracks are assumed to have the same length $2a$ and the same strike direction, which coincides with the $X$-axis. All the crack surfaces are assumed to be stress-free. Cracks are distributed periodically

with the spacings of $d_X$ and $d_Y$ in the $X$ and $Y$ directions, respectively. The number density of cracks $\nu$ is given by $\nu=1/d_X d_Y$. The cracks are distributed along the line $Y=(j-1)d_Y$ ($j$=1, ⋯, $N$), where $N$ is the number of crack arrays in the $Y$ direction. We determine the $X$-coordinate of the centre of cracks in each array $p_j+ld_X$ ($0\le p_j<d_X$, $j$=1,⋯, $N$, $l$=0, ±1, ±2,⋯) by generating $N$ uniform random numbers between 0 and 1, which are multiplied by $d_X$.

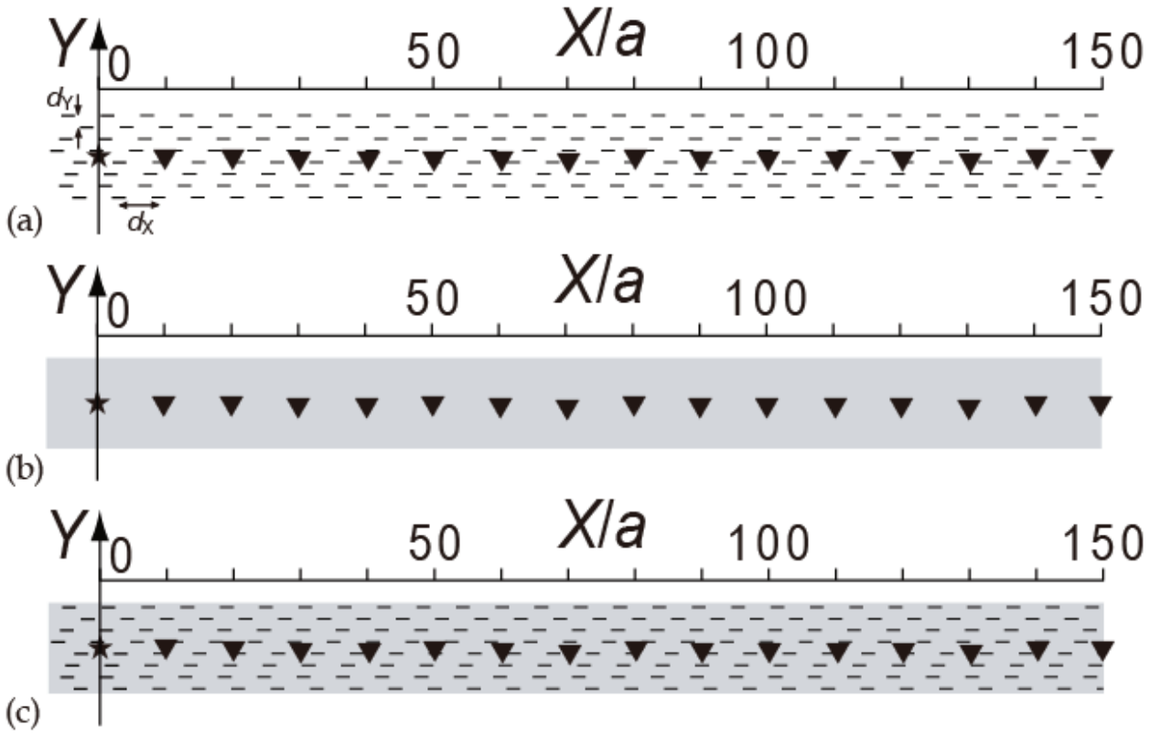


Fig. 1. Five models of a fault zone. A star denotes an isotropic line source located at the centre of the fault zone at $X$=0. The row of triangles represents observation stations. The spacing in the $Y$ direction between the stations and the centre of the fault zone is 0.425$a$, where $a$ is half the crack length for fault zone models with distributed cracks and normalization length for those without cracks. (a) An example of Model (1). Cracks are distributed periodically with the density of $\nu a^2$=0.1. The crack spacings are $d_X$=5.88$a$ and $d_Y$=1.7$a$ in the $X$ and $Y$ directions, respectively. (b) Examples of fault zone Models (2), (3) and (4). The grey-shaded zone is an anisotropic zone, a low-velocity zone and an anisotropic low-velocity zone in Models (2), (3) and (4), respectively. The width of the grey-shaded zone is $h$=13.6$a$. The elastic constant of the anisotropic zone is $c_{2323}$=0.711$\mu$ for Model (2), where $\mu$ is the rigidity. The shear wave velocity $\beta$ and density $\rho$ of the low-velocity zone for Model (3) are $\beta/\beta_0$=0.8 and $\rho/\rho_0$=0.93, where $\beta_0$ and $\rho_0$ are shear wave velocity and density of the surrounding rocks, respectively. The elastic constant, density and rigidity of the anisotropic low-velocity zone for Model (4) are $c_{2323}$=0.711$\mu$, $\rho/\rho_0$=0.93 and $\mu/\mu_0$=0.6, respectively, where $\mu_0$ is the rigidity of the surrounding rocks. (c) An example of Model (5). The grey-shaded zone is a low-velocity zone. The width, shear wave velocity and density of the low-velocity zone are $h$=13.6$a$, $\beta/\beta_0$=0.8 and $\rho/\rho_0$=0.93, respectively. The same crack distribution is assumed as Model (1) in (a)

2. A single anisotropic zone whose elastic constant is equivalent to that of the crack distribution Model (1) at the long-wavelength limit (Fig. 1b). The elastic constant $c_{2323}$ is derived for the case of normal incidence to the crack surfaces by Murai (2007) as

$$\frac{c_{2323}}{\mu} = \frac{(2-\pi\nu a^2)^2}{4}, \tag{1}$$

where $\mu$ is the rigidity and the coordinate system ($X$, $Y$) is redefined as ($x_1$, $x_3$) for notation of the anisotropic media. The width of the cracked zone $h$ is defined as $h=Nd_Y$.

3. A low-velocity zone with $\beta/\beta_0$ and $\rho/\rho_0$, where $\beta$ is the shear wave velocity and $\rho$ is the density, and the subscript 0 denotes the surrounding rocks (Fig. 1b). The rigidity $\mu$ is obtained by $\mu=\rho\beta^2$.
4. An anisotropic low-velocity zone (Fig. 1b). We assume the same elastic constant of $c_{2323}/\mu$ as Model (2) and the same $\beta/\beta_0$, $\rho/\rho_0$ and $\mu/\mu_0$ as Model (3).
5. A low-velocity zone with densely distributed parallel cracks (Fig. 1c). We assume the same crack distribution as Model (1) and the same $\beta/\beta_0$, $\rho/\rho_0$ and $\mu/\mu_0$ as Model (3).

## 3. Formulation

The seismic source displacement field is represented as a superposition of homogeneous and inhomogeneous plane waves propagating at discrete angles. This discretization results from a periodicity assumption in the description of the source (Bouchon & Aki, 1977).

The harmonic waves radiated from a line source in an infinite homogeneous medium can be represented as a continuous superposition of homogeneous and inhomogeneous plane waves. Therefore, the displacement $u_s$ in wavenumber domain from the seismic source located at the origin of the coordinate system ($x$, $y$) can be written in the form,

$$u_s(x,y) = \int_{-\infty}^{\infty} f(s,y)e^{isx}ds, \tag{2}$$

where $i$ is the imaginary unit and $s$ is the $x$-component of the wavenumber. The time factor $\exp(-i\omega t)$ is omitted for brevity, where $\omega=k\beta$, $k$ is the wavenumber. When such sources distribute along the $x$-axis at equal interval $\Delta x_s$, eq.(2) is reduced to

$$u_{ss}(x,y) = \frac{2\pi}{\Delta x_s}\sum_{l=-\infty}^{\infty} f(s_l,y)e^{is_l x}, \tag{3}$$

according to Bouchon & Aki (1977), where $u_{ss}$ is the displacement from periodically distributed sources and $s_l=2\pi l/\Delta x_s$. If the series converges, eq.(3) can be approximated by the finite sum equation

$$u_{ss}(x,y) = \frac{2\pi}{\Delta x_s}\sum_{l=-N_d}^{N_d} f(s_l,y)e^{is_l x}. \tag{4}$$

Thus the seismic source displacement field is represented as a superposition of the discrete plane waves.

Now we give the wavenumber a small imaginary part to remove the singularities of $f(k, y)$ as

$$k = k_R + ik_I. \tag{5}$$

The resulting attenuation is used to minimize the influence of the neighboring fictitious sources. The effect of the imaginary part of the wavenumber can be removed from the final time domain solution. When the solution in wavenumber domain by using the complex wavenumber is denoted by $U(k)$, the solution in time domain $u(t)$ is obtained through the relation

$$u(t) = \frac{\beta}{2\pi} e^{\beta k_I t} \int_{-\infty}^{\infty} U(k) e^{-i\beta k_R t} dk. \tag{6}$$

We consider an isotropic line source. The displacement field radiated from a source is written as

$$u_s(x, y) = \frac{i}{4} H_0^{(1)}(kR), \tag{7}$$

where $R^2=x^2+y^2$, and $H_0^{(1)}(\cdots)$ is the Hankel function. We employ the relation by Morse & Feshbach (1953)

$$H_0^{(1)}(kR) = \frac{1}{\pi} \int_{-\infty}^{\infty} \frac{\exp[i\{\sqrt{k^2 - s^2}\,|y| + sx\}]}{\sqrt{k^2 - s^2}} ds. \tag{8}$$

Then eq.(7) can be written as

$$u_s(x, y) = \frac{i}{4\pi} \int_{-\infty}^{\infty} \frac{\exp[i\{\sqrt{k^2 - s^2}\,|y|]}{\sqrt{k^2 - s^2}} e^{isx} ds. \tag{9}$$

Therefore, $f(k, y)$ in eq.(2) can be determined to be

$$f(s, y) = \frac{i}{4\pi} \frac{\exp[i\{\sqrt{k^2 - s^2}\,|y|]}{\sqrt{k^2 - s^2}}. \tag{10}$$

For the anisotropic media of Models (2) and (4), eq.(10) is modified as

$$f(s, y) = \frac{i}{4\pi} \sqrt{\frac{\mu}{c_{2323}}} \frac{\exp\left[i\sqrt{\frac{\mu}{c_{2323}}}\sqrt{k^2 - s^2}\,|y|\right]}{\sqrt{k^2 - s^2}}. \tag{11}$$

The velocity contrast can be introduced easily because we have only to treat plane waves. The wave field in a fault zone can be calculated by the wave propagator method (Kennett, 1983) or the reflection and transmission operator method (Kennett, 1984) by use of the discretization results. Moreover we can calculate the displacement field radiated from a seismic source embedded in a fault zone for Models (1) and (5) on the basis of this expansion because the seismic wave propagation in a zone of densely distributed parallel cracks for

incident plane waves can be calculated by the method introduced by Murai & Yamashita (1998).

## 4. Synthetic seismograms

We consider the fault zone Model (1) as shown in Fig. 1(a). We assume 8 crack arrays which are 1.7$a$ apart each other in the $Y$ direction. A seismic source is located at (0, 5.95$a$) and is assumed to be isotropic. Observation stations are located along the line $Y$=6.375$a$. Thus both the source and the stations are located near the centre of the fault zone. The synthetic seismograms for 15 stations in the range 10$a$≤$X$≤150$a$ are shown in Fig. 2. The seismograms in the time domain are obtained by the Fourier transform of the wavenumber domain solutions for 134 wavenumbers in the range from $ka$=0.025 to $ka$=3.35. We use the Ricker wavelet as the source time function; the characteristic nondimensional wavenumber of the wavelet, $k_c a$, is assumed to be 1.0. Fig. 2 shows the wave trains scattered by cracks following the direct wave at only the stations neighboring the source. Moreover the wave trains contain the dominant high wavenumber components. Thus we cannot simulate the relatively long-period fault zone trapped waves for the events with various focal distances. Because the cracked zone of Model (1) is equivalent to a single anisotropic zone at the low wavenumber limit, we consider the fault zone Model (2) as shown in Fig. 1(b). The elastic constant $c_{2323}$ is obtained as $c_{2323}$=0.711$\mu$ for $\nu a^2$=0.1 by eq.(1). The width of the cracked zone $h$ is defined as $h$=$Nd_Y$. The synthetic seismograms for 15 stations in the range 10$a$≤$X$≤150$a$ are shown in Fig. 3. We can see neither scattered waves nor fault zone trapped waves.

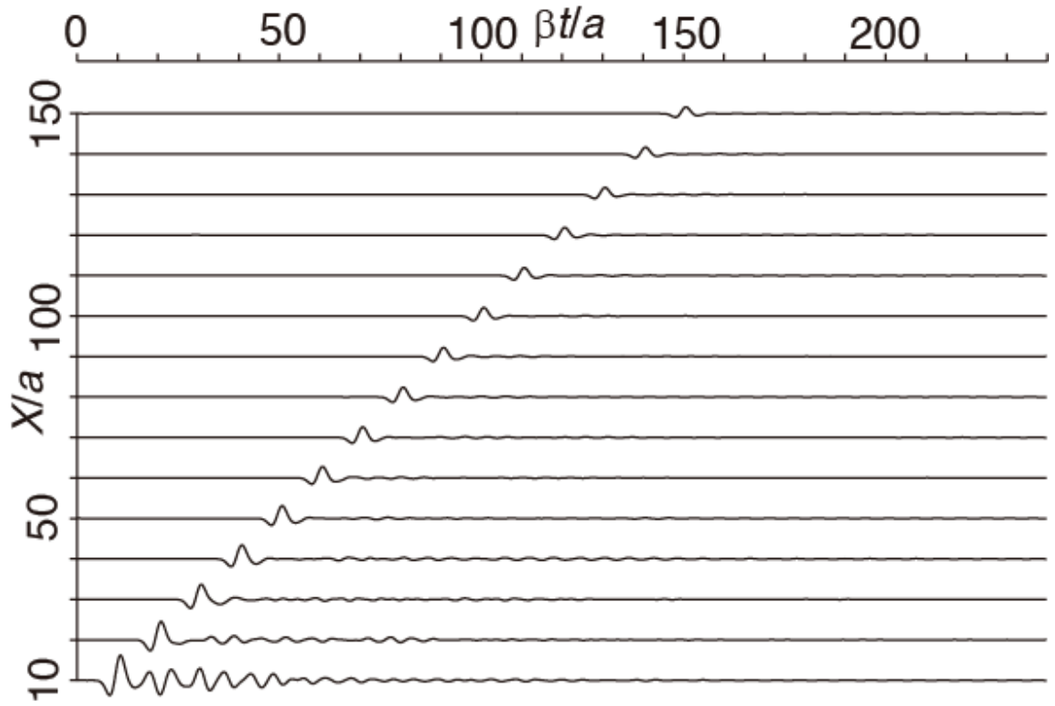


Fig. 2. The synthetic seismograms calculated for the fault zone Model (1) of crack distribution shown in Fig. 1(a). The characteristic nondimensional wavenumber of Ricker wavelet, $k_c a$, is 1.0

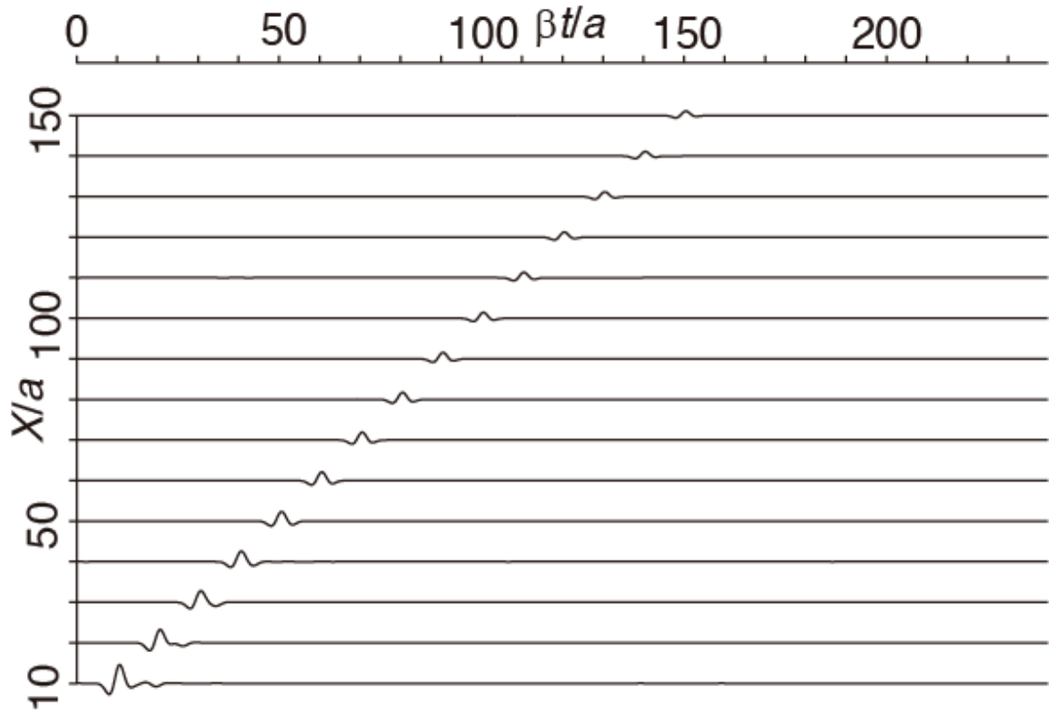


Fig. 3. The synthetic seismograms calculated for the fault zone Model (2) of the single anisotropic zone shown in Fig. 1(b). $k_c a$ is assumed to be 1.0

The results of Models (1) and (2) suggest that a low-velocity fault zone is necessary to excite trapped waves. Actually a fault zone is characterized as a low-velocity zone as stated in section 1. It is certainly the case that the phase velocity decreases remarkably in the fault zone for the waves propagating normal to the cracks, but the velocity is almost the same as the shear wave velocity of the matrix for the waves propagating parallel to the cracks in the assumed Models (1) and (2) because we consider only SH waves. The low-velocity zone is, however, considered to be attributed to fault gouge (Mooney & Ginzburg, 1986), which might include not only the parallel cracks but also randomly oriented microcracks; a velocity reduction is observed for the waves propagating to any direction.

We now consider the low-velocity fault zone Model (3) as shown in Fig. 1(b). The width of the low-velocity fault zone is the same as that of the anisotropic fault zone Model (2). The shear wave velocity and density of the low-velocity zone are assumed to be $\beta/\beta_0$=0.8 and $\rho/\rho_0$=0.93, respectively, which correspond to the rigidity of $\mu/\mu_0$=0.6. The synthetic seismograms are shown in Fig. 4. This figure shows the relatively long-period wave trains with relatively large amplitude closely following the direct waves with small amplitude at all the stations. These long-period wave trains are understood as trapped waves in the low-velocity zone because they are observed only in the low-velocity fault zone. Thus we can simulate the relatively long-period fault zone trapped waves. Therefore, an actual fault zone is considered to be low-velocity. In addition, Fig. 4 shows the headwaves refracted along the cross-fault material contrast, which are observed in actual fault zones as stated in section 1 (Ben-Zion & Malin, 1991; Hough et al., 1994). We cannot see scattered waves because there is no crack in the fault zone.

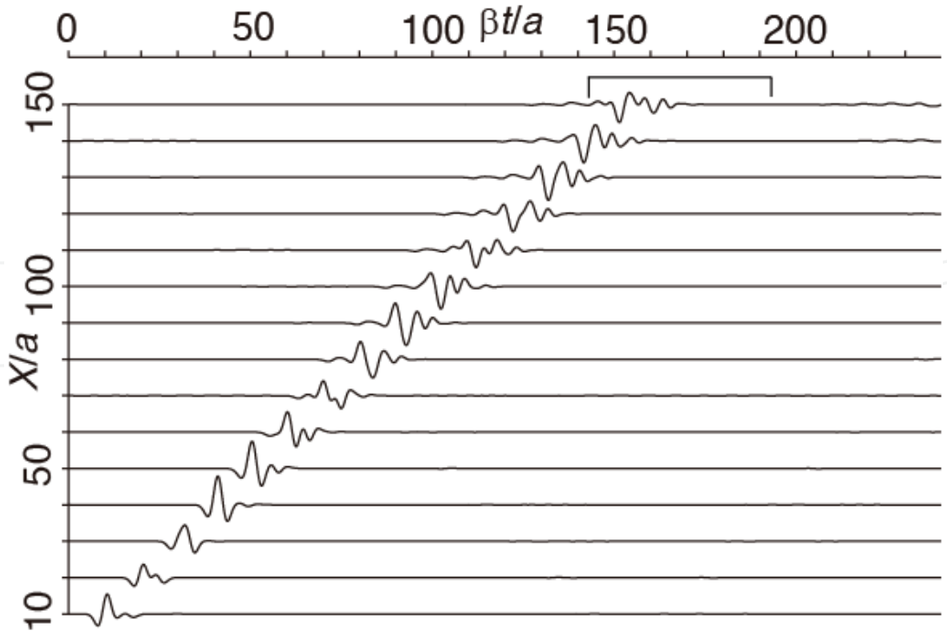


Fig. 4. The synthetic seismograms calculated for the fault zone Model (3) of the single low-velocity zone shown in Fig. 1(b). $k_c a$ is assumed to be 1.0. The bracket denotes a spectral time window of $50\beta/a$ including the direct wave and the trapped wave trains for the seismogram of the station at $X$=150$a$. The amplitude spectra are shown in Fig. 7(a)

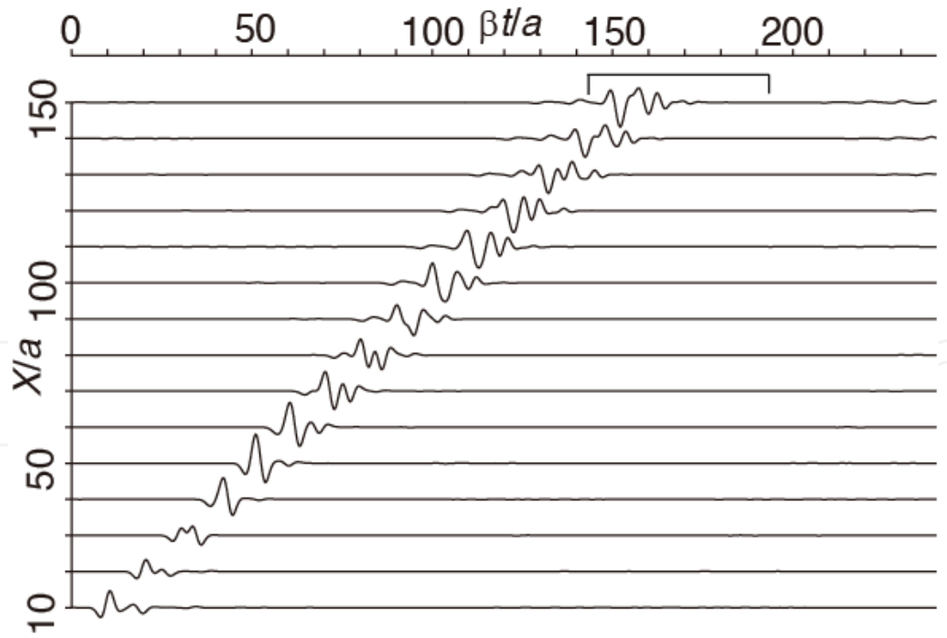


Fig. 5. The synthetic seismograms calculated for the fault zone Model (4) of the single anisotropic low-velocity zone shown in Fig. 1(b). $k_c a$ is assumed to be 1.0. The bracket denotes a spectral time window of $50\beta/a$ including the direct wave and the trapped wave trains for the seismogram of the station at $X$=150$a$. The amplitude spectra are shown in Fig. 7(b)

Next, we consider the anisotropic low-velocity fault zone Model (4) as shown in Fig. 1(b) in order to consider the effect of parallel crack distribution. The width of the anisotropic low-velocity fault zone is the same as those of Models (2) and (3). The elastic constant $c_{2323}$, density and rigidity of the anisotropic low-velocity zone are assumed to be $c_{2323}=0.711\mu$, $\rho/\rho_0=0.93$ and $\mu/\mu_0=0.6$, respectively as the same for Models (2) and (3), which correspond to the crack density of $\nu a^2=0.1$ and shear wave velocity of $\beta/\beta_0=0.8$. The synthetic seismograms are shown in Fig. 5. This figure shows the same characteristics as Fig. 4: we can observe the refracted headwaves, the direct waves with relatively small amplitude and the trapped wave trains and cannot see scattered waves. This is because the crack length is assumed to be much smaller than the incident wavelength in the anisotropic zone.

Finally, we consider a low-velocity zone with densely distributed parallel cracks (Fig. 1c) in order to consider the effect of a wavenumber dependence of the crack interactions in a fault zone. The width of the low-velocity fault zone is the same as those of Models (2), (3) and (4). We assume the same crack distribution as Model (1) and the same shear wave velocity and density of the low-velocity zone as Model (3): $\nu a^2=0.1$, $\beta/\beta_0=0.8$ and $\rho/\rho_0=0.93$ are assumed.

The synthetic seismograms are shown in Fig. 6. This figure shows the same characteristics as Figs. 4 and 5 of the wave propagation in a low-velocity fault zone. In addition, we can observe the wave trains scattered by cracks following the fault zone trapped waves.

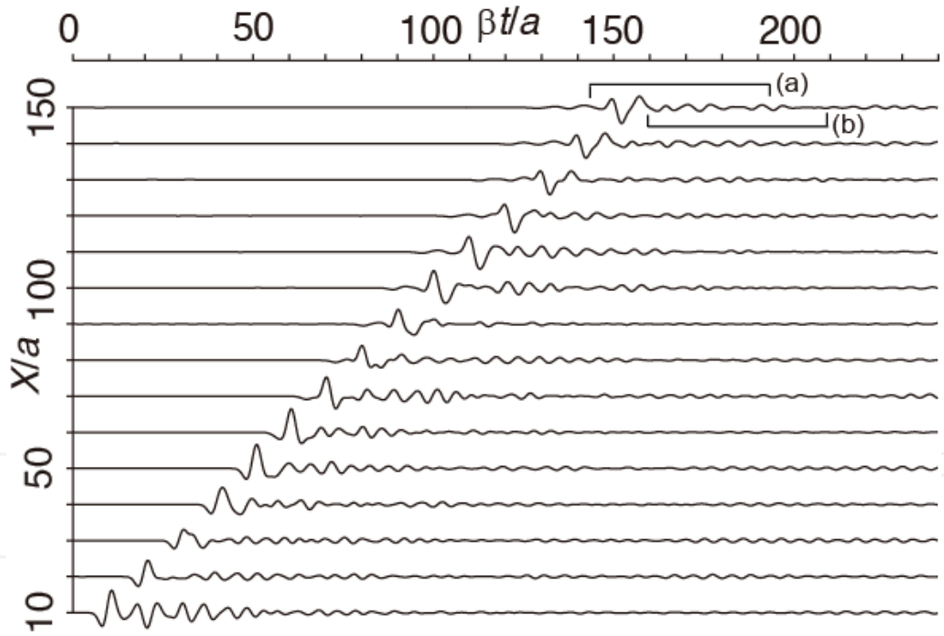


Fig. 6. The synthetic seismograms calculated for the fault zone Model (5) of the low-velocity zone with densely distributed parallel cracks shown in Fig. 1(c). We assume the same crack distribution as for Fig. 2. $k_c a$ is assumed to be 1.0. The brackets denote spectral time windows of $50\beta/a$ for the seismogram of the station at $X=150a$. The time window (a) is including the direct wave, the wave trains trapped in the low-velocity zone and the waves scattered by cracks whereas the time window (b) is including only the scattered wave trains. The amplitude spectra for the time windows (a) and (b) are shown in Figs. 7(c) and (d), respectively

## 5. Spectral analyses

In this section, we make a short analysis on the amplitude spectra for the fault zone trapped waves calculated in the previous section. Figs. 7(a) and (b) show the amplitude spectra calculated for the fault zone Models (3) and (4) illustrated in Fig. 1(b), respectively, and Figs. 7 (c) and (d) show those for Model (5) illustrated in Fig. 1(c). The amplitude spectra $U$ are calculated by the following procedure. First, we compute the synthetic seismograms with the Ricker wavelet as the source time function; we assume the 4 Ricker wavelets whose $k_c a$ are 0.25, 0.5, 1.0 and 2.0. Next, we calculate the amplitude spectrum for each Ricker wavelet source time function in a time window of $50\beta/a$ using a cosine type window with $5\beta/a$ edge length. The spectral windows are shown in Figs. 4, 5 and 6 for the seismograms of the station at $X=150a$ with $k_c a=1.0$ as an example. Finally, the amplitude spectrum for each Ricker wavelet is normalized by that of each source time function to eliminate the contribution of source spectra. The amplitude spectra $U(k)$ are calculated for the wavenumber range $2k_c/3 \le k \le 4k_c/3$ from each Ricker wavelet with the characteristic wavenumber of $k_c$. Because 4 Ricker wavelets with $k_c a=0.25$, 0.5, 1.0 and 2.0 are assumed, the amplitude spectra are discontinuous at $ka=1/3$, $2/3$ and $4/3$.

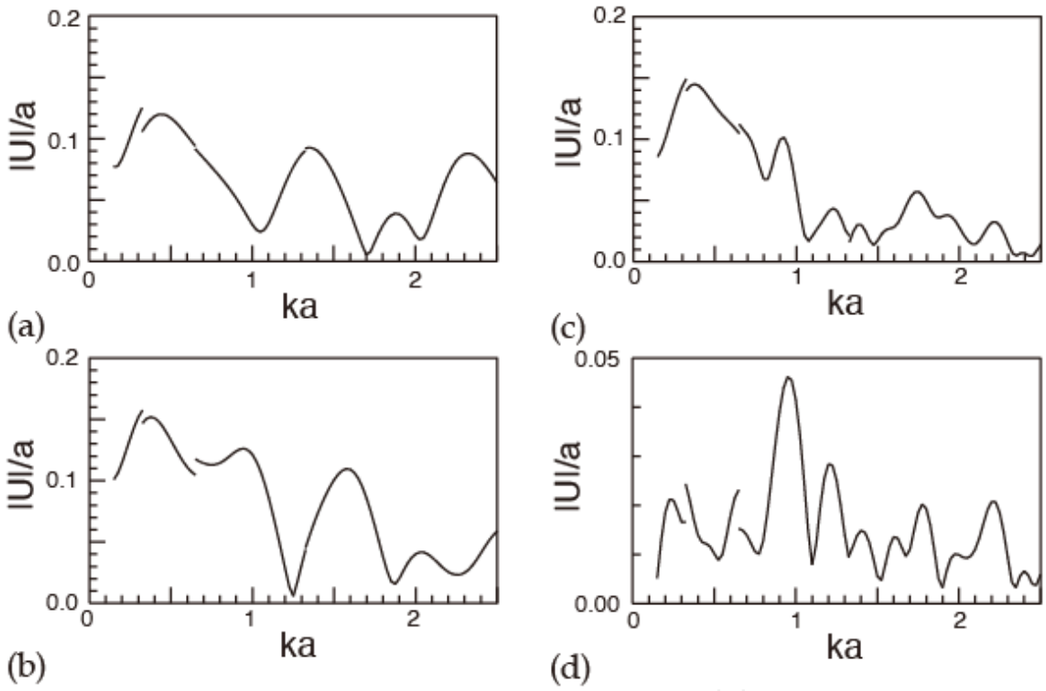


Fig. 7. The normalized amplitude spectra $|U(ka)|/a$ calculated for the seismograms of the observation station at $X=150a$. $|U(ka)|/a$ are calculated for the wavenumber ranges of $0.150 \le ka \le 0.325$, $0.325 \le ka \le 0.650$, $0.650 \le ka \le 1.325$ and $1.325 \le ka \le 2.650$ from Ricker wavelet source time functions with $k_c a=0.25$, 0.5, 1.0 and 2.0, respectively. (a) The amplitude spectra calculated for the fault zone Models (3) illustrated in Fig. 1(b). (b) The amplitude spectra calculated for the fault zone Models (4) illustrated in Fig. 1(b). (c) The amplitude spectra calculated for the fault zone Models (5) illustrated in Fig. 1(c). The amplitude spectra in (a), (b) and (c) correspond to the direct wave and the trapped wave trains of the seismogram in Figs. 4, 5 and 6, respectively. (d) The same as in (c) except for corresponding to the wave trains scattered by cracks

Fig. 7(a) shows the normalized amplitude spectra for the low-velocity fault zone Model (3). This figure corresponds to the seismogram of the station at $X$=150$a$ in Fig. 4. The amplitude spectra show the prominent peak at $ka$=0.45, which is understood to be formed by the waves trapped in the low-velocity zone. Fig. 7(b) shows the normalized amplitude spectra for the anisotropic low-velocity fault zone Model (4), which correspond to the seismogram of the station at $X$=150$a$ in Fig. 5. This figure also shows the prominent peaks at $ka$=0.375 and 0.95 formed by the fault zone trapped waves. The spectral peak split into two peaks because the interference of resonated waves in the layer occurs at the wavenumbers different from that for the isotropic medium due to the wave speed depending on the propagation direction. Fig. 7(c) shows the normalized amplitude spectra for the fault zone Model (5) of the low-velocity zone with densely distributed parallel cracks, which correspond to the seismogram in the time window (a) of the station at $X$=150$a$ in Fig. 6. The amplitude spectra show the prominent peaks at $ka$=0.325 in relatively low wavenumber range and at around $ka$=1.0 in relatively high wavenumber range. The low-wavenumber spectral peak is considered to be formed by the waves trapped in the low-velocity zone because it is seen in Figs. 7(a) and (b). The peak amplitude in the low wavenumber range is higher in Fig. 7(c) than that in Fig. 7(a). Moreover the existence of the cracks lowers the peak wavenumber at which the amplitude spectra take the peak value in the low wavenumber range. These phenomena occur because the crack distribution lowers the overall rigidity and velocity in the fault zone. The high-wavenumber spectral peak is caused only for the fault zone Model (5). Now we calculate the amplitude spectra for the wave trains scattered by cracks in order to investigate the high-wavenumber peak. The spectral time window (b) is denoted by the bracket in Fig. 6 for $k_c a$=1.0 as an example. Fig. 7(d) shows the normalized amplitude spectra for the scattered waves. This figure shows the most prominent peak at around $ka$=1.0 in relatively high

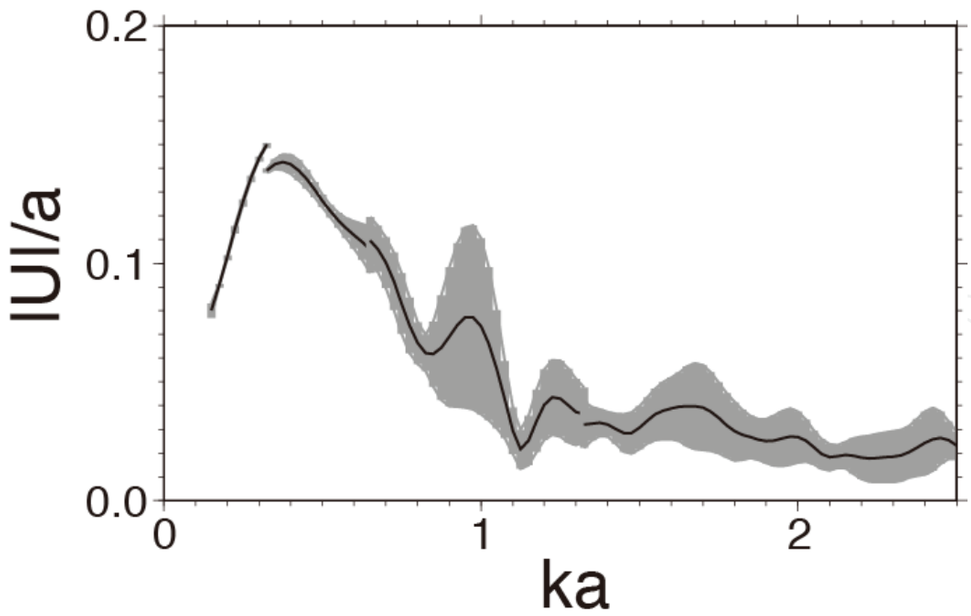


Fig. 8. The normalized amplitude spectra calculated from the direct wave and the trapped and scattered wave trains of the synthetic seismograms for the fault zone Model (5) illustrated in Fig. 1(c). Solid curve and grey-shaded range represent the mean values and the standard deviations of 201 stations in the range 100$a$≤$X$≤150$a$ along the line $Y$=6.375$a$

wavenumber range, therefore it is understood to be formed by scattered waves. This means that we can estimate the crack length in a fault zone from the peak frequency in the high frequency range if the spectral peak caused by the waves scattered by cracks is observable.

We calculate synthetic seismograms and amplitude spectra from the direct wave and the trapped wave trains of 201 stations in the range $100a \leq X \leq 150a$ along the line $Y=6.375a$ of the fault zone Models (5) illustrated in Fig. 1(c) in order to investigate the spatial variation of the spectral peaks in relatively low and high wavenumber ranges. Fig. 8 shows the mean values and the standard deviations of the normalized amplitude spectra for the 201 stations. The amplitude of the low-wavenumber spectral peak is not attenuated among these observation stations because the long-period wave trains are trapped and propagating without geometrical spreading in the low-velocity zone. On the other hand, the amplitudes of the high-wavenumber spectral peak fluctuate greatly among stations although it is seen at most of the stations. The mean values of the amplitude spectra show the low-wavenumber peak is caused at $ka=0.375$ and the amplitude is $|U|/a=0.143$, and the high-wavenumber peak is at $ka=0.975$ with the amplitude of $|U|/a=0.077$.

## 6. Wave propagation in a fault zone containing densely distributed parallel cracks

In the previous section, the amplitude spectra show the prominent peaks in relatively low and high wavenumber ranges for the fault zone Model (5) of the low-velocity zone with densely distributed parallel cracks when both the source and stations are located near the centre of the fault zone. In this section, we investigate the amplitude spectra for the fault zone Model (5) with crack distributions different from that illustrated in Fig. 1(c). We assume the same width, shear wave velocity and density of the low-velocity zone as shown in Fig. 1(c). First, we consider 10 crack distributions with the same crack spacings of $d_X$ and $d_Y$, which correspond to the same crack density of $\nu a^2=0.1$ as shown in Fig. 1(c). Each of the above 10 crack distributions is determined by generating an independent sequence of random numbers in order to determine the $X$-coordinates of the centre of cracks. For each model, the mean values of the amplitude spectra are obtained by averaging over 201 stations by the same procedure as stated in the previous section. Each of 10 curves in Fig. 9(a) shows the mean values of the normalized amplitude spectra from the 201 stations for each of 10 models. The spectral peaks in relatively low and high wavenumber ranges are detected from each of the 10 curves in Fig. 9(a). The mean values and the standard deviations of both the wavenumbers and amplitudes of the spectral peaks for all the 10 models are computed. The low-wavenumber peak is caused at $ka=0.38\pm0.01$ and the amplitude is $|U|/a=0.142\pm0.001$, and the high-wavenumber peak is at $ka=0.94\pm0.16$ with the amplitude of $|U|/a=0.077\pm0.016$.

Next, we assume the crack densities of $\nu a^2=0.075$ and 0.05 lower than above for the fault zone Model (5) although the same width, shear wave velocity and density of the low-velocity zone are assumed. We assume 2 sets of $d_X$ and $d_Y$ for each crack density: $d_X=5.88a$ and $d_Y=2.38a$ (Fig. 10a), and $d_X=7.84a$ and $d_Y=1.7a$ (Fig. 10b) for $\nu a^2=0.075$, and $d_X=5.88a$ and $d_Y=3.97a$ (Fig. 11a), and $d_X=11.76a$ and $d_Y=1.7a$ (Fig. 11b) for $\nu a^2=0.05$. We consider 10 crack distributions for each model with the different crack spacings, i.e., 20 distributions for each crack density in total.

Each of 20 curves in Fig. 9(b) shows the mean values of the normalized amplitude spectra from the 201 stations for each of 20 models for the crack density of $\nu a^2$=0.075. The spectral peaks in relatively low and high wavenumber ranges are detected from each of the 20 curves in Fig. 9(b) and the mean values and the standard deviations of both the wavenumbers and amplitudes of the spectral peaks for all the 20 models are computed. The low-wavenumber peak is caused at $ka$=0.38±0.02 and the amplitude is $|U|/a$=0.137±0.001, and the high-wavenumber peak is at $ka$=0.98±0.14 with the amplitude of $|U|/a$=0.071±0.012. Each of 20 curves in Fig. 9(c) shows the mean values of the normalized amplitude spectra from the 201 stations for each of 20 models for the crack density of $\nu a^2$=0.05. The low-wavenumber peak is caused at $ka$=0.39±0.01 and the amplitude is $|U|/a$=0.131±0.002, and the high-wavenumber peak is at $ka$=0.92±0.13 with the amplitude of $|U|/a$=0.074±0.011.

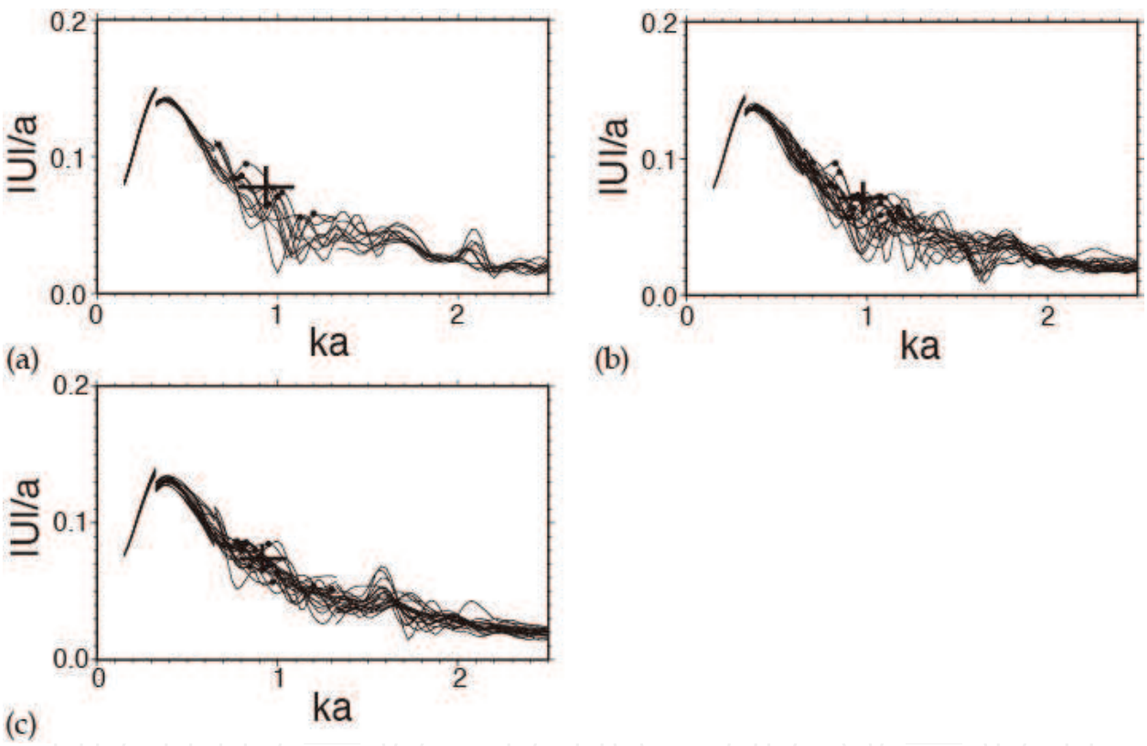


Fig. 9. The mean values of the normalized amplitude spectra obtained by averaging over 201 stations for each fault zone Model (5). The high-wavenumber spectral peak detected from each curve is denoted by a dot. The standard deviations of both the wavenumber and amplitude of the high-wavenumber spectral peaks for all the models are denoted by bars. The intersecting point of the bars represents the mean values. (a) Each of 10 curves shows the mean values of the amplitude spectra for each of 10 models with $d_X$=5.88$a$ and $d_Y$=1.7$a$ ($\nu a^2$=0.1). (b) Each of 20 curves shows the mean values of the amplitude spectra for each of 20 models with $\nu a^2$=0.075. Ten of 20 curves show the models with $d_X$=5.88$a$ and $d_Y$=2.38$a$ and other 10 of 20 show the models with $d_X$=7.84$a$ and $d_Y$=1.7$a$. (c) Each of 20 curves shows the mean values of the amplitude spectra for each of 20 models with $\nu a^2$=0.05. Ten of 20 curves show the models with $d_X$=5.88$a$ and $d_Y$=3.97$a$ and other 10 of 20 show the models with $d_X$=11.76$a$ and $d_Y$=1.7$a$

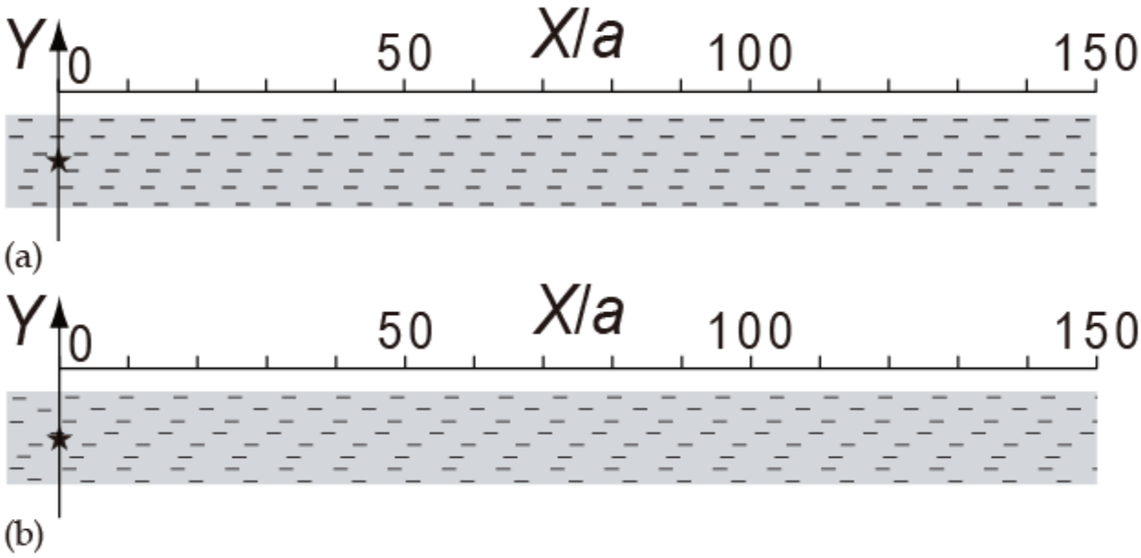


Fig. 10. The same as Fig. 1(c) except for $\nu a^2$=0.075. (a) An example of fault zone Model (5) with $d_X$=5.88$a$ and $d_Y$=2.38$a$. (b) An example of fault zone Model (5) with $d_X$=7.84$a$ and $d_Y$=1.7$a$

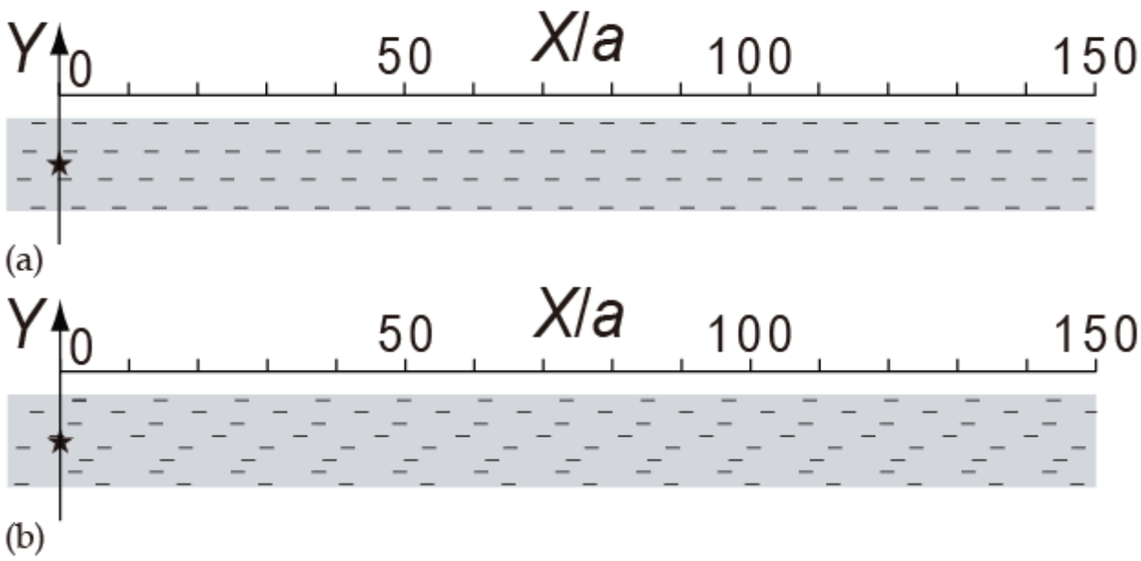


Fig. 11. The same as Fig. 10 except for $\nu a^2$=0.05. (a) An example of fault zone Model (5) with $d_X$=5.88$a$ and $d_Y$=3.97$a$. (b) An example of fault zone Model (5) with $d_X$=11.76$a$ and $d_Y$=1.7$a$

We summarize the crack density dependence of the amplitudes of the spectral peaks in the relatively low and high wavenumber ranges (Fig. 9) in Figs. 12(a) and (b), respectively. Fig. 12(a) shows the larger amplitude for the higher crack density as for the spectral peaks at around $ka$=0.4 in the relatively low wavenumber range. On the other hand, the amplitudes of the spectral peaks at around $ka$=1.0 in the relatively high wavenumber range fluctuate greatly among models of crack distribution and show no clear dependency on the crack density (Fig. 12b). Thus the spectral peak amplitude in the low-wavenumber range becomes larger relative to that in the high-wavenumber range for higher crack density. The spectral

peak amplitude in the low-wavenumber range does not depend only on the crack density but also depends on the shear wave velocity, density and the width of the low-velocity zone because it is formed by the waves trapped in the low-velocity zone. Therefore, the crack density cannot be estimated from it alone. However, it will be possible to estimate the crack density by modelling a fault zone to satisfy the observed spectral peak amplitudes in both the low and high wavenumber ranges because the spectral peak amplitude in the high-wavenumber range can be used as the reference to that in the low-wavenumber range.

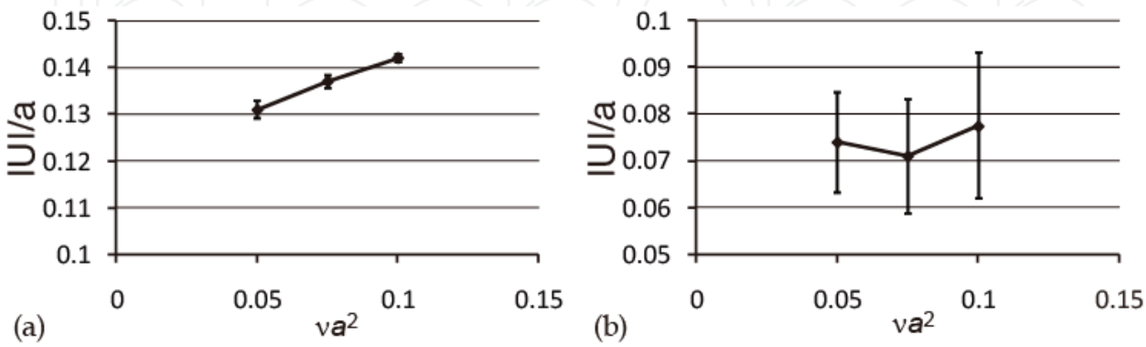


Fig. 12. Crack density dependence of the spectral peak amplitudes. (a) and (b) show the spectral peak amplitudes in the relatively low ($ka$~0.4) and high ($ka$~1.0) wavenumber ranges, respectively

## 7. Interpretation of the amplitude spectra observed in the fault zone of the 1992 Landers earthquake

In this section, we compare the amplitude spectra observed by Li et al. (1994) in the fault zone of the 1992 Landers earthquake with the synthesis calculated for the fault zone Model (5) of the low-velocity zone with densely distributed parallel cracks. Li et al. (1994) deployed a seismic array across the fault trace of the M7.4 Landers earthquake of June 28, 1992. They found the distinct wave train with a relatively long period following the direct S waves that shows up only when both the stations and the events are close to the fault trace. The coda-normalized amplitude spectra show a spectral peak at 3-4Hz (Fig. 13). They interpreted the long-period wave trains as a seismic guided wave trapped in a low-velocity fault zone and estimated a waveguide width of about 180m and a shear wave velocity of 2.0-2.2 km/s. The amplitude spectra show also a spectral peak of the high frequency at 8-15Hz (Fig. 13). The observed amplitude spectra can be simulated by modelling the fault zone as Model (5) of the low-velocity zone with densely distributed parallel cracks in this study (e.g., Fig. 7c). Although Li et al. (1994) did not infer the origin of the high frequency spectral components, each of the peaks in the low and high wavenumber range is interpreted from our simulation to be formed by the waves trapped in the low-velocity zone and the waves scattered by the cracks, respectively.

First, we try to estimate the dominant crack length in the fault zone. Because the amplitude spectra show the prominent peak at around $ka$=1.0 in relatively high wavenumber range, we can estimate the crack length by using the estimated shear wave velocity of 2.0 km/s and the observed frequency of 10Hz of the spectral peak at the high frequency by Li et al. (1994).

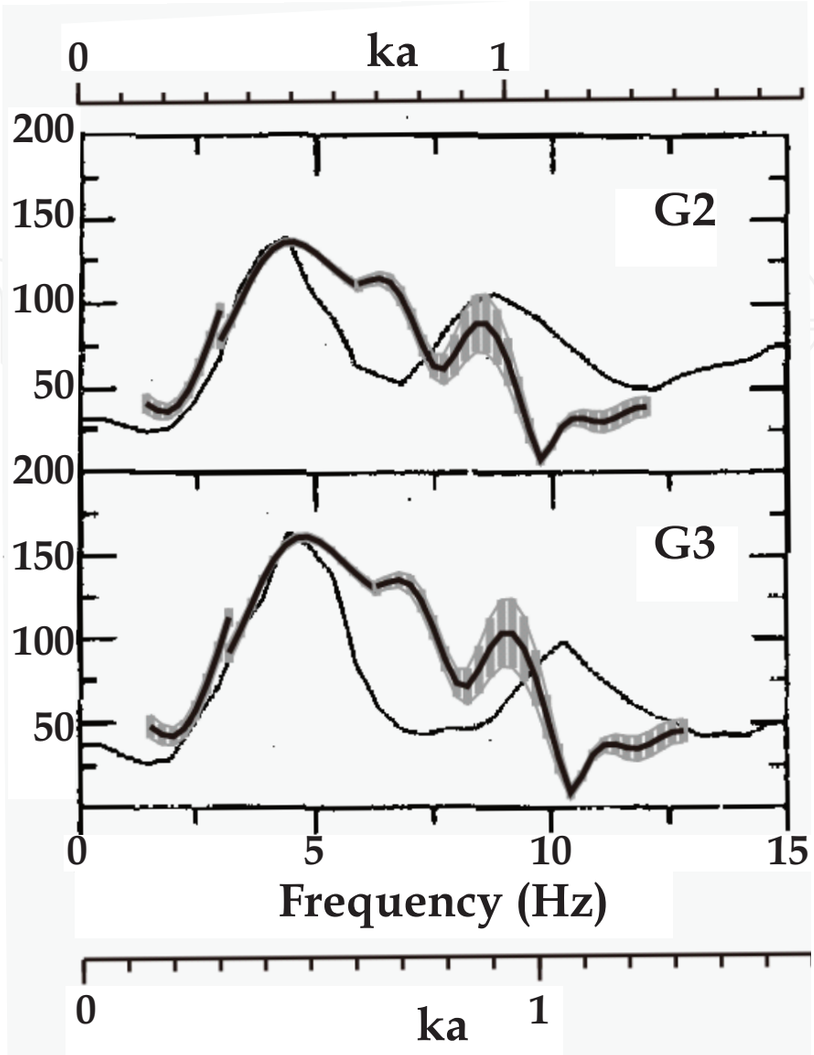


Fig. 13. The amplitude spectra observed in the fault zone of the 1992 Landers earthquake by Li et al. (1994) (thin curves) [reproduced by permission of American Geophysical Union.] and those calculated from the direct wave and the trapped and scattered wave trains of the synthetic seismograms for the fault zone Model (5) with $\beta/\beta_0$=0.7, $\rho/\rho_0$=0.895, $h$=8.4$a$, $d_X$=3.97$a$, $d_Y$=2.1$a$ and $\nu a^2$=0.12 (bold curves). Thin curves represent the coda-normalized amplitude spectra of horizontal components (parallel to the mainshock fault trace) of seismograms recorded at stations (G2 and G3) located close to the mainshock fault trace for an event occurred within the fault zone. Bold curves and grey-shaded ranges represent the mean values and the standard deviations of 201 stations in the range 100$a$≤$X$≤150$a$ along the line $Y$=3.5$a$ for an isotropic line source located at the centre of the fault zone (0, 3.15$a$), respectively. The low-velocity zone is bounded by lines of $Y$=7.35$a$ and $Y$=-1.05$a$

The dominant crack length is estimated as

$$2a \sim \frac{2}{k} = \frac{2\beta}{\omega} = \frac{\beta}{\pi f} = \frac{2000(\mathrm{m/s})}{10(\mathrm{Hz})\pi} = 60\mathrm{m}, \tag{12}$$

where $\omega$ is the angular frequency and $f$ is the frequency of the spectral peak at the high frequency. Next, we try to estimate the crack density in the fault zone by simulating the observed amplitude spectra. Because Li et al. (1994) estimated the shear wave velocities of the low-velocity fault zone and the surrounding rock as 2.0-2.2 km/s and 3.0 km/s, respectively, we assume the shear wave velocity and density of the low-velocity zone as $\beta/\beta_0$=0.7 and $\rho/\rho_0$=0.895 in our simulation. The peak wavenumber of the relatively low-wavenumber range becomes lower for a low-velocity zone with the larger width. The amplitude spectra also depend on the crack density. The spectral peak amplitudes in the low-wavenumber range become larger for the higher crack density and its dependency is heavier for a fault zone with the smaller width. On the other hand, the spectral peak amplitudes at around $ka$=1.0 show considerable variation among the spatial distributions of cracks and the observation stations even if the same crack density is assumed and do not obviously depend on the crack density. We find an example of the fault zone model which satisfies both of the spectral peak amplitudes in the low and high wavenumber ranges as the width of the low-velocity zone of $h$=8.4$a$ and the crack spacings in the $X$ and $Y$ directions of $d_X$=3.97$a$ and $d_Y$=2.1$a$, respectively (Fig. 13). Thus the width of the low-velocity zone is estimated as 252m by eq.(12), which is a little larger than 180m estimated by Li et al. (1994), and the crack density is $\nu a^2$=0.12, which represents dense distribution of parallel cracks in the fault zone.

## 8. Conclusion

We compute the synthetic seismograms of the displacement field radiated from a seismic source embedded in a fault zone. We assume following five models as a fault zone and investigate SH wave propagation in a 2-D elastic medium.

1. A zone of densely distributed parallel cracks.
2. An anisotropic zone whose elastic constants are equivalent to those of the crack distribution model (1) at the long-wavelength limit.
3. A low-velocity zone.
4. An anisotropic low-velocity zone.
5. A low-velocity zone with densely distributed parallel cracks.

For Models (1) and (2), we cannot simulate the fault zone trapped waves. We therefore have to consider a low-velocity fault zone to excite trapped waves. For Models (3), (4) and (5), the seismograms show fault zone trapped waves and headwave refracted along the cross-fault material contrast. For Model (5), the seismograms show the waves scattered by cracks in addition to the fault zone trapped waves. Next, we investigate the amplitude spectra. We calculate the amplitude spectrum for each Ricker wavelet source time function in a time window including the direct wave and the trapped and scattered wave trains. For Models (3), (4) and (5), the amplitude spectra show the prominent peak in relatively low-wavenumber range corresponding to the fault zone trapped waves. For Model (4), the low-wavenumber spectral peak splits into two peaks because the interference of resonated waves in the layer occur at the wavenumbers different from that for the isotropic medium due to the wave speed depending on the propagation direction. For Model (5), the amplitude spectra show the prominent peak at $ka$~1.0 in relatively high-wavenumber range corresponding to the scattered waves in addition to the low-wavenumber spectral peak corresponding to the fault zone trapped waves.

Finally, we investigate the amplitude spectra for Model (5) of the low-velocity zone with densely distributed parallel cracks. The amplitude spectra depend on the width and velocity of the low-velocity zone and the crack density. We compare the amplitude spectra observed by Li et al. (1994) in the fault zone of the 1992 Landers earthquake with the synthesis calculated for the fault zone Model (5). We find an example of the fault zone model which satisfies both of the spectral peak amplitudes in the low and high wavenumber ranges. Thus we can estimate the dominant crack length as about 60m and the crack density as $\nu a^2$=0.12, which represents dense distribution of parallel cracks in the fault zone. Such an estimated model might be ambiguous because the spectral peak amplitudes in the high-wavenumber range show considerable variation among the spatial distributions of cracks and the observation stations even if the same crack density is assumed. Therefore, a statistical analysis will be required for results calculated for many crack distributions and observation stations.

We assumed cracks distributed periodically with the same spacings in a fault zone but such distribution is not realistic. We have to consider randomly distributed cracks in a fault zone for example. If the crack length has some distribution, the broader spectral peak will be observed. The dominant crack length can, however, be estimated in this case as well. Actually the frequency band of the seismic observation is limited. The length of the cracks can not be estimated by the proposed method when the crack length is shorter than the observable seismic wavelengths. Therefore, the crack length estimated in this study should be regarded as the dominant length in the range of the observable wavelengths and might reflect the distribution of relatively long cracks. Because the distribution of the relatively long cracks is considered to be effective to the large earthquake occurrence, the estimation stated here is significant to the monitoring of the preparation process of large earthquakes. It is a future work that the present computations will include the effects of microcrack distribution as the macroscopic parameters such as $Q$ value. Although we investigate SH wave propagation in a 2-D elastic medium, this is the first theoretical study of elastic wave propagation in a low-velocity zone with densely distributed cracks without the assumption of low wavenumber approximation. The results obtained here will be the basis to estimate crack distribution in a fault zone. Further study is required to extend the present computations to 3-D simulations.

## 9. Acknowledgment

I thank Prof. T. Yamashita for helpful comments. This study was partly supported by a Grant-in-Aid from the Ministry of Education, Science, Sports and Culture of Japan (project 19540434) and the Earthquake Research Institute (ERI), the University of Tokyo, cooperative research programs (2006-W-06, 2007-W-05, 2008-W-03, 2009-W-01, 2010-W-04 and 2011-W-03). For this study, I have used the computer systems of Earthquake Information Center of ERI.

## 10. References

Ben-Zion, Y. & Malin, P. (1991). San Andreas fault zone head waves near Parkfield, California. Science, Vol.251, No.5001, (March 1991), pp. 1592-1594, ISSN 0036-8075.

Bouchon, M. & Aki, K. (1977). Discrete wave-number representation of seismic-source wave fields. Bull. seism. Soc. Am., Vol.67, No.2, (April 1977), pp. 259-277, ISSN 0037-1106.

Hough, S. E., Ben-Zion, Y., & Leary, P. (1994). Fault-zone waves observed at the southern Joshua Tree earthquake rupture zone. Bull. seism. Soc. Am., Vol.84, No.3, (June 1994), pp. 761-767, ISSN 0037-1106.

Kennett, B. L. N. (1983). Seismic wave propagation in stratified media, Cambridge University Press, ISBN 0-521-23933-8, Cambridge.

Kennett, B. L. N. (1984). Reflection operator methods for elastic waves II - composite regions and source problems. Wave Motion, Vol.6, No.4, (July 1984), pp. 419-429, ISSN 0165-2125.

Kurita, T. (1975). Attenuation of shear waves along the San Andreas fault zone in central California. Bull. seism. Soc. Am., Vol.65, No.1, (February 1975), pp. 277-292, ISSN 0037-1106.

Leary, P. C., Li, Y.-G., & Aki, K. (1987). Observation and modelling of fault-zone fracture seismic anisotropy - I. P, SV and SH travel times. Geophys. J. R. astr. Soc., Vol.91, No.2, (November 1987), pp. 461-484, ISSN 0952-4592.

Li, Y.-G., Aki, K., Adams, D., & Hasemi, A. (1994). Seismic guided waves trapped in the fault zone of the Landers, California, earthquake of 1992. J. geophys. Res., Vol.99, No.B6, (June 1994), pp. 11705-11722, ISSN 0148-0227.

Li, Y.-G. & Leary, P. C. (1990). Fault zone trapped seismic waves. Bull. seism. Soc. Am., Vol.80, No.5, (October 1990), pp. 1245-1271, ISSN 0037-1106.

Li, Y.-G., Leary, P. C., & Aki, K. (1987). Observation and modelling of fault-zone fracture seismic anisotropy - II. P-wave polarization anomalies. Geophys. J. R. astr. Soc., Vol.91, No.2, (November 1987), pp. 485-492, ISSN 0952-4592.

Malin, P. E., Waller, J. A., Borcherdt, R. D., Cranswick, E., Jensen, E. G., & Van Schaack, J. (1988). Vertical seismic profiling of Oroville microearthquakes: velocity spectra and particle motion as a function of depth. Bull. seism. Soc. Am., Vol.78, No.2, (April 1988), pp. 401-420, ISSN 0037-1106.

Mooney, W. D. & Ginzburg, A. (1986). Seismic measurements of the internal properties of fault zones. Pageoph, Vol.124, No.1/2, (January 1986), pp. 141-157, ISSN 0033-4553.

Morse, P. M. & Feshbach, H. (1953). Methods of theoretical physics. McGraw-Hill, ISBN 007043316X, New York.

Murai, Y. (2007). Scattering attenuation, dispersion and reflection of SH waves in two-dimensional elastic media with densely distributed cracks. Geophys. J. Int., Vol.168, No.1, (January 2007), pp. 211-223, ISSN 0956-540X.

Murai, Y. & Yamashita, T. (1998). Multiple scattering of SH waves by imperfectly bonded interfaces with inhomogeneous strengths. Geophys. J. Int., Vol.134, No.3, (September 1998), pp. 677-688, ISSN 0956-540X.

Tchalenko, J. S. (1970). Similarities between shear zones of different magnitudes. Geol. Soc. Am. Bull., Vol.81, No.6, (June 1970), pp. 1625-1640, ISSN 0016-7606.

Tchalenko, J. S. & Berberian, M. (1975). Dasht-e Bayaz fault, Iran: earthquake and earlier related structures in bed rock. Geol. Soc. Am. Bull., Vol.86, No.5, (May 1975), pp. 703-709, ISSN 0016-7606.

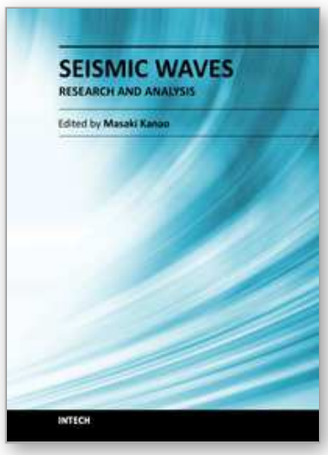


**Seismic Waves - Research and Analysis**

Edited by Dr. Masaki Kanao

ISBN 978-953-307-944-8
Hard cover, 326 pages
**Publisher** InTech
**Published online** 25, January, 2012
**Published in print edition** January, 2012

The importance of seismic wave research lies not only in our ability to understand and predict earthquakes and tsunamis, it also reveals information on the Earth's composition and features in much the same way as it led to the discovery of Mohorovicic's discontinuity. As our theoretical understanding of the physics behind seismic waves has grown, physical and numerical modeling have greatly advanced and now augment applied seismology for better prediction and engineering practices. This has led to some novel applications such as using artificially-induced shocks for exploration of the Earth's subsurface and seismic stimulation for increasing the productivity of oil wells. This book demonstrates the latest techniques and advances in seismic wave analysis from theoretical approach, data acquisition and interpretation, to analyses and numerical simulations, as well as research applications. A review process was conducted in cooperation with sincere support by Drs. Hiroshi Takenaka, Yoshio Murai, Jun Matsushima, and Genti Toyokuni.



**InTech Europe**
University Campus STeP Ri
Slavka Krautzeka 83/A
51000 Rijeka, Croatia
Phone: +385 (51) 770 447
Fax: +385 (51) 686 166
www.intechopen.com

**InTech China**
Unit 405, Office Block, Hotel Equatorial Shanghai
No.65, Yan An Road (West), Shanghai, 200040, China
中国上海市延安西路65号上海国际贵都大饭店办公楼405单元
Phone: +86-21-62489820
Fax: +86-21-62489821

IntechOpen